Research Square

Preprints are preliminary reports that have not undergone peer review.
They should not be considered conclusive, used to inform clinical practice,
or referenced by the media as validated information.

A dimensionless framework for epidemic management: Linking behavioural adaptation to hospital demand

Felix Mairanowski
SmairGmbH https://orcid.org/0000-0002-3678-0198
Below Denis
denisbelow@hotmail.de
Alexianer Krankenhaus https://orcid.org/0009-0004-3282-8387

Research Article

Keywords: mathematical modelling, similarity theory, epidemic management, contact reduction, hospital demand

Posted Date: November 12th, 2026

DOI: https://doi.org/10.21203/rs.3.rs-11694499/v1

License: This work is licensed under a Creative Commons Attribution 4.0 International License.
Read Full License

Additional Declarations: The authors declare no competing interests.

A dimensionless framework for epidemic management: Linking behavioural adaptation to hospital demand.

Denis Below (1,*), ***Felix Mairanowski*** *(2)*

(1) Alexianer Clinic, Berlin, Germany (ORCID: 0009-0004-3282-8387)

(2) Smair Tech. GmbH, Berlin, Germany (ORCID: 0000-0002-3678-0198)

(1) Corresponding author. Denis Below. Email Address: denisbelow@hotmail.de

Keywords: mathematical modelling; similarity theory; epidemic management; contact reduction; hospital demand.

Abstract

This work presents a methodological framework for epidemic management rather than a pathogen-specific model. The COVID-19 pandemic provides an opportunity to calibrate and test the approach across diverse regions and waves.

We propose an analytical framework that links behavioural responses to hospital demand. At its core is a single behavioural parameter that captures how populations reduce contacts during outbreaks. Using data from multiple COVID-19 waves across different regions, we show that this parameter reflects age structure and socioeconomic conditions.

The framework reveals that stronger behavioural responses consistently reduce peak hospitalisations. The scaling relation is validated against empirical data from 50 US jurisdictions, capturing a substantial component of the observed variation in peak hospitalisation burden. The resulting dimensionless control operator quantifies the reduction in peak demand under non-pharmaceutical interventions, independent of absolute regional capacity.

This establishes a unified, parameterisable tool for rapid healthcare forecasting across current and future respiratory pathogens.

1. Introduction

Healthcare infrastructure managers and policymakers face critical choices during infectious disease surges: initiating non-pharmaceutical interventions, balancing socio-economic costs against the risk of ICU saturation, and deploying immunisation logistics. The COVID-19 pandemic underscored that these decisions must often be made under severe uncertainty, with critical care networks operating at or beyond capacity.

Classical multi-compartment models (e.g., SIR, SEIR) are widely used [1,2], but they rely on high-dimensional parameter spaces and intensive numerical simulations. This computational overhead restricts their utility as agile, real-time decision support tools. Moreover, behavioural adaptations — mask use, distancing, voluntary contact reduction — are typically treated as static external inputs rather than as dynamic feedback operators within the transmission equations.

To address these limitations, this paper develops an analytically solvable macro-scale framework for operational decision support in critical healthcare infrastructure. The primary output is not the infection curve itself, but the peak hospitalisation demand — the quantity that determines whether the healthcare system becomes saturated and triage protocols must be activated. The framework also provides analytical elasticities to quantify how interventions (behavioural measures and vaccination) affect this peak demand. The core innovation is a macroscopic behavioural contact reduction parameter, lambda, which integrates multi-faceted population compliance into a single, interpretable rate. By generating explicit analytical solutions, the framework enables immediate evaluation of intervention scenarios without numerical calibration ensembles.

The model separates behavioural mitigation (lambda) from intrinsic transmission intensity (k), while incorporating mass vaccination and structural population heterogeneity through piecewise-smooth sectioning. Epidemic progression is governed by two dimensionless similarity complexes: the transmissibility invariant ($\Pi_1 = k/\lambda$) and the normalised time ($\Pi_2 = \lambda*t$). The healthcare-demand scaling additionally involves the ratio $g = \lambda/\gamma$, which couples the behavioural and clinical timescales. When these invariants match between populations, their trajectories collapse onto a universal curve up to time rescaling — analogous to the Buckingham Pi theorem and hydrodynamic scaling laws [3].

A distinctive feature of the framework is the explicit treatment of age structure in healthcare demand. Because severe outcomes are concentrated among older cohorts, an effective age modifier A(eff) is introduced, with weights derived from the age gradient of case fatality. This

allows the model to distinguish between populations with different demographic compositions and to estimate peak bed demand under the assumption that beds are allocated according to age-specific fatal risk.

Importantly, the framework is not pathogen-specific. While calibrated on COVID-19 — which provided an unparalleled high-resolution natural experiment — it is re-parameterisable for other respiratory pathogens. We also note that lambda is not a statistical artefact but reflects real socio-demographic structure, correlating with socioeconomic conditions rather than with age distribution, which our regional diagnostics confirm to be statistically independent. We derive analytical elasticities for healthcare infrastructure, showing that peak hospital demand and behavioural adaptation can be deterministically predicted.

This study treats the COVID-19 pandemic as a large-scale epidemiological experiment, focusing exclusively on methodological development

2. Methodology

2.1. Mathematical Framework and Model Assumptions

To capture the macroscopic behaviour of the epidemic wave while maintaining analytical tractability, we utilize a deterministic, reduced-form compartment framework. Unlike standard state-space representations that prioritize active infectious counts, the primary state variable tracked herein is the cumulative infection incidence. Within this formulation, individuals transitioning out of the susceptible compartment are immediately removed from the active mixing pool due to terminal recovery, sustained isolation, or mortality, thereby terminating their contribution to the transmission chain.

The dynamic evolution of the system is governed by a set of coupled differential equations. To assess the core propagation mechanisms, we differentiate between behavioural adaptation under non-pharmaceutical interventions and the direct depletion of the hosting pool via immunization campaigns. The general structure of the model is formulated as follows [4]:

$$\frac{dS}{dt} = S(- \lambda — \frac{\alpha v}{1-\alpha v * t}) \qquad (1)$$

$$\frac{dI}{dt} = k_0 * \frac{S*I}{N} — \gamma I \qquad (2)$$

where S(t) and I(t) denote the instantaneous sub-populations of susceptible and infected individuals within a total closed population N, respectively. The parameter k_0 represents the

intrinsic, unmitigated transmission rate day^{-1}, while γ accounts for the clearance or recovery rate day^{-1}.

The coefficient λ day^{-1}is an effective macroscopic behavioural scaling parameter describing the rate of population-level contact reduction. Its value may change during an epidemic wave as behavioural responses and containment measures change. In the present formulation, λ is therefore treated as a regime-dependent parameter rather than as an immutable population constant.

Rather than assuming static mixing, $\boldsymbol{\lambda}$ quantifies the rate at which the susceptible population insulates itself or is removed from the active contact network via risk-induced behavioural modifications and statutory containment measures. This parameterization aligns with foundational concepts in behavioural epidemiology, where contact topologies dynamically compress in response to perceived public health risks. For the subsequent analytical derivations of wave thresholds and asymptotic limits, we evaluate the limiting case where $\boldsymbol{\gamma = 0}$, reflecting early-stage epidemic acceleration where recovery kinetics do not yet restrict the expanding infected pool.

1. Here, S represents the effective number of hosts susceptible to the given specific viral strain. Crucially, as demonstrated by contemporary longitudinal serological tracking and neutralization assays, the magnitude of S at the initialization node of each novel wave segment remains functionally independent of the cumulative infection headcount from preceding outbreaks. Because rapid antigenic drift and evolutionary immune escape mechanisms systematically erode legacy antibody barriers, the replacing pathogen encounters a virtually restored susceptible phase space. Consequently, this complete decoupling of the susceptible-infected feedback loop allows the multi-wave timeline to be solved analytically as a sequence of independent wave segments.[5,6,7]

2. 2.2. Analytical Solution for the Susceptible Pool

Integration of the effective susceptible population balance in Equation (1) yields an exact analytical trajectory:

$$S = S_0 * e^{-\lambda t} * (1 - \alpha v * t) \qquad (3)$$

where $\mathbf{S_0}$ signifies the initial susceptible population at the onset of the designated wave. This product form demonstrates an elegant separation of scales: the exponential term models the continuous, risk-driven behavioural contraction of the contact network, whereas the linear term captures the steady, time-dependent depletion induced by a uniform vaccination campaign characterized by a daily coverage rate **v** (day^{-1} and an efficacy factor α.

2.3. Trajectory and Limits of the Infected Population

By inserting the analytical solution for S(t) (Equation 3) into the infectious population rate equation (Equation 2), the system collapses into a closed-form differential equation. In the baseline scenario prior to the deployment of vaccination (αv = 0), the growth trajectory can be expressed in terms of the relative infected percentage of the host population (i = 100 * I / N) via the displacement variable Δi. Under the analytical boundary condition γ = 0, the cumulative growth of the wave simplifies to:

$$\Delta i = i_0 * exp\left[\frac{k}{\lambda}\left(1 - e^{-\lambda t}\right)\right] \quad (4) \quad \text{where}$$

$$\Delta i = i - i_f \quad (5) \quad ,$$

i_f – the value of i for the previous wave of the epidemic at the time the new strain emerged,

Here, i_f represents the residual baseline infection percentage inherited from the preceding evolutionary wave at the structural boundary where the novel variant emerges. Mathematically, Eq. 4 takes the exact structural form of classical Gompertz growth kinetics [8]. Inspection of Equation (4) confirms that the intrinsic dynamics are governed by two distinct control criteria: the temporal attenuation scale **λ** and the dimensionless intensity ratio k/λ, which dictates the total magnitude of the outbreak.

The effective transmission coefficient k is scaled to the initial susceptible fraction according to

$$k = k_0 * \frac{S_0}{N} \quad (6)$$

To enforce universality across varying scale factors, we introduce the standardization constraint:

$$i_0 = \frac{100}{N}. \quad (7)$$

The temporal position of the maximum inflection point, corresponding to the peak daily acceleration of the wave (t_{max}), is analytically determined by:

145 $t_{max}= \frac{\ln(\frac{k}{\lambda})}{\lambda}$ (8),

146 The corresponding maximum value of the daily incidence increment ($\mathbf{j_{max}}$) scales as follows:

147 $j_{max} = \frac{100}{N} \lambda * exp(\frac{k}{\lambda} -1)$ (9)

148 The ultimate asymptotic boundary of the infected fraction as the temporal horizon extends is
149 given by:

150 $\lim_{t\to\infty} \Delta i = i_0 * exp\left[\frac{k}{\lambda}\right]$ (10)

151 **2.4. Dimensionless Scaling Groups and Similarity Criteria**

152 To establish a scale-invariant representation of cross-regional epidemics without vaccination,
153 the governing equations can be mapped onto a set of three independent dimensionless Π-
154 groups derived via dimensional analysis:

155 $\Pi_1 = k / \lambda$ (ratio of transmission to behavioural adaptation) (11)

156 $\Pi_2 = \lambda t$ (dimensionless time) (12)

157 Here, Π_1 denotes the structural intensity index (balancing intrinsic transmission against
158 behavioural mitigation velocity), Π_2 defines the normalized intrinsic time scale. adaptation.
159 When mapped into this coordinate space {Π_1, Π_2, }, epidemiological trajectories from highly
160 heterogeneous geographical regions condense into invariant functional profiles, validating the
161 application of hydrodynamic similarity principles to population-level transmission dynamics.

162 **2.5. Superposition of Variant Trajectories and Wave Packets**

163 To model the long-term, multi-wave behaviour of the epidemic without relying on complex,
164 continuous non-linear competition frameworks, we treat the sequential emergence of novel
165 viral strains as a linear superposition of independent dynamic states. This formulation
166 assumes that successive variants (such as the transitions from the ancestral strain to Alpha,
167 and subsequently to Delta) do not directly compete for the same instantaneous host pool
168 because their peak activities are separated in time.

169 Un3-1-der the assumption of decoupled dynamics, the total relative increase in infected
170 individuals can be mathematically approximated by the sum of individual wave contributions.

When a secondary strain emerges at a distinct chronological timestamp t_2, characterized by its own transmission coefficient k_2 and behavioural mitigation scale $\boldsymbol{\lambda_2}$, the combined trajectory is expressed as:

$$\Delta i = i_0 * \{exp\left[\frac{k_1}{\lambda_1}\left(1 - e^{-\lambda_1 t}\right)\right] + exp\left[\frac{k_2}{\lambda_2}\left(1 - e^{-\lambda_2 (t-t_2)}\right)\right]\} \qquad (13),$$

This two-strain superposition profile effectively replicates the empirical transition dynamics observed during major evolutionary shifts. In practical engineering and data analysis workflows, this piecewise strategy is highly justified. Because a replacing variant typically gains momentum at a boundary where the transmission cycle of the preceding strain has already decayed to near-zero levels, the multi-wave timeline can be computed piece-by-piece as a sequence of consecutive, isolated wave packets. This approach maintains absolute simplicity, allowing the entire system to be modeled using standard spreadsheet tools without solving coupled systems of non-linear differential equations

2.6. Model Calibration and Parametric Scaling Laws

The operational state of the dynamic framework is fully determined by three primary parameters: the effective transmission coefficient k, the behavioural contact reduction scale $\boldsymbol{\lambda}$ and the total closed population N.

The parameter k serves as a scaling factor that couples the intrinsic biological transmissibility of the pathogen with the initial susceptible fraction of the host population. For the ancestral SARS-CoV-2 strain propagating during the first wave, the baseline transmission coefficient was calibrated using the following empirical relation, which accounts for the initial scale of the population pool:

$$k=0.355 - 0.035*\ln\left(\frac{10^6}{N}\right), \qquad (14)$$

When a novel variant emerges with a higher intrinsic transmission capacity, the system undergoes a parametric shift. Rather than reconstructing the entire framework, the baseline coefficient is adjusted using a structural scaling law that reflects the relative evolutionary advantage of the new strain:

$$\frac{k_2}{\lambda_2} = \frac{k_1}{\lambda_1} + \ln(\varepsilon), \qquad (15)$$

where $\boldsymbol{\varepsilon}$ represents the relative transmissibility index of the invading variant compared to the baseline ancestral pathogen. For example, for the Alpha variant ($\varepsilon \approx 1.6$), this relation shifts

the transmission coefficient to $k_1 \approx 0.37$ day^{-1}, while for the highly transmissible Delta variant ($\varepsilon \approx 2.0$), the coefficient scales up to $k_2 \approx 0.385$ day^{-1}. This functional adjustment ensures that a proportional increase in biological transmission intensity translates directly into a predictable, mathematically consistent shift in the system's baseline operating parameter.

3. Results

Daily COVID-19 case counts (7-day moving average) were obtained from the Johns Hopkins University CSSE repository. [9]

The model was validated against empirical data. Since the attenuation parameter λ is locked analytically by the universal limit(Equation (10), $\alpha v = 0$)

$$\lambda = k/\ln(\Delta i_\infty / i_0) \quad (16)$$

the model operates no free empirical parameters.

Furthermore, to account for the genetic evolution of the pathogen during the autumn-winter surge, the virus transmissibility for the second wave was scaled deterministically.(Equations (14) and (15)) .

3.1. Baseline Model Verification Across Divergent Demographic Matrices

To verify the predictive capability and structural robustness of the deterministic closed-form framework prior to introducing active control interventions, the analytical trajectory was validated against the historical datasets of Rhode Island, New York State, and Brazil. For all baseline scenarios for all baselines, $\Pi_3 = 0$, with k scaled by population size *N*, the behavioural deceleration parameter λ day^{-1}.The temporal origin ($t = 0$) for each system was locked strictly to the detection of the first confirmed index case to enforce independent boundary conditions. Both analytical and empirical daily velocities are expressed as the daily fraction of new infections (% per day), with empirical curves computed via a 7-day finite difference step ($\Delta i / \Delta t$) to eliminate weekly data-logging artifacts.

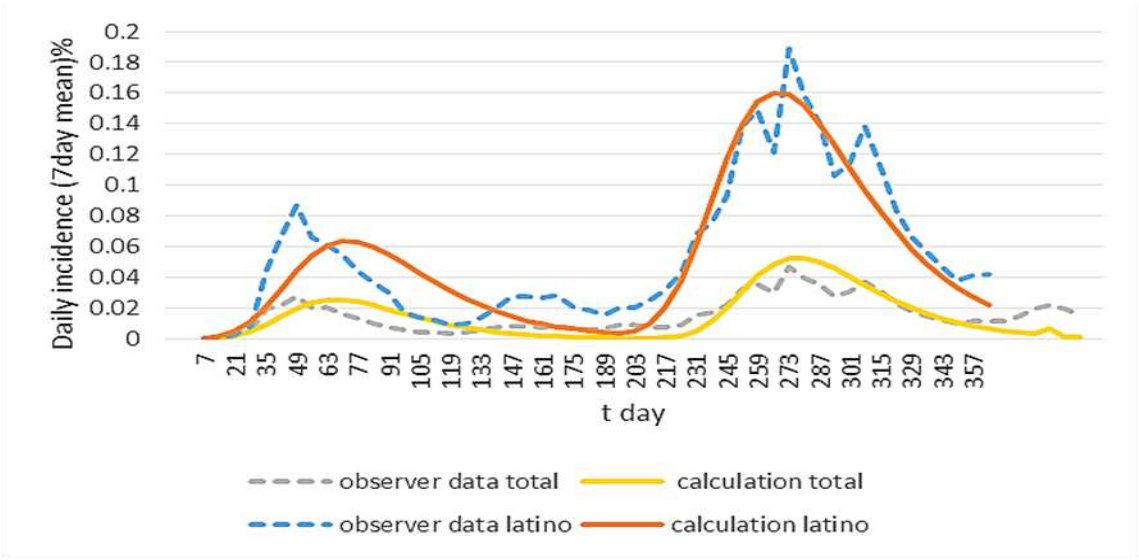


Figure 1. Observed and modeled daily infection incidence (i (%)) (7-day rolling mean) versus physical time t (days) for the total population (N = 1.057 10^6),(grey dashed and yellow solid lines) and the Hispanic/Latino demographic subgroup ((N = 1.59 *10^5) [10],(blue dashed and orange solid lines) of Rhode Island.

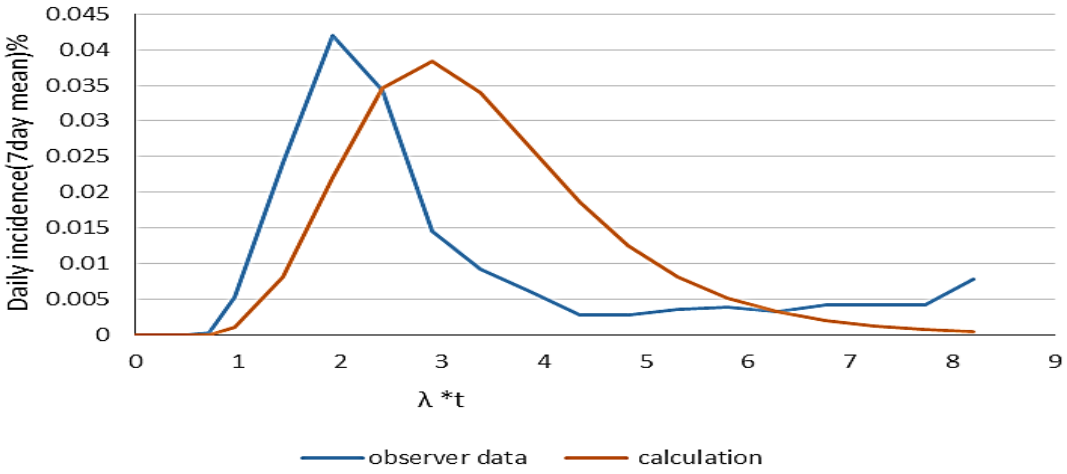


Figure 2. Daily infection incidence fraction (% per day) (7-day rolling mean) versus scaled dimensionless epidemiological time $\tau = \lambda^* t$ for New York State (N = 19.4* 10^6). The blue solid line represents real-world empirical observer data and the orange solid line represents the analytical model calculation (λ= 0.0345 day^{-1})

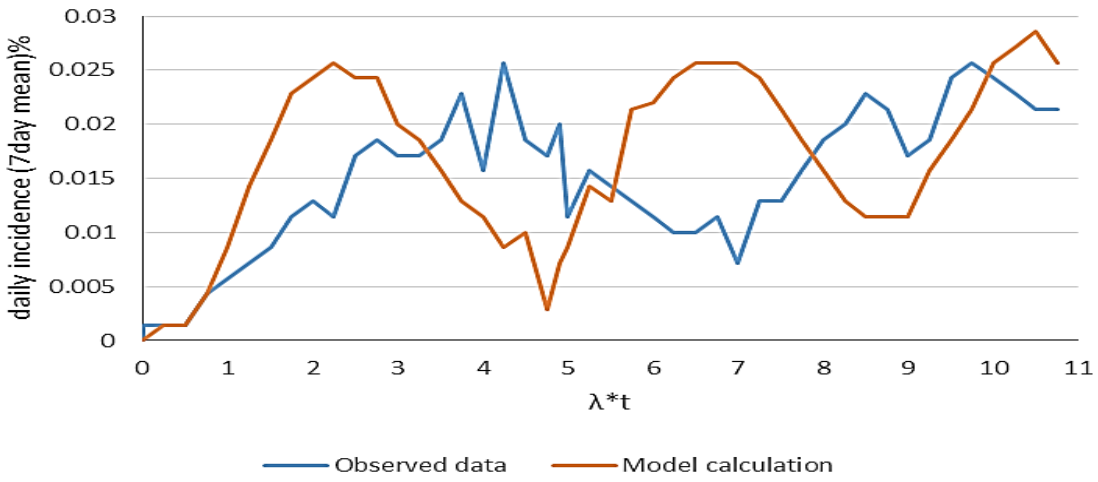


Figure 3. Multi-wave daily infection incidence i (%) (7-day rolling mean) versus scaled dimensionless epidemiological time $\tau = \lambda^*t$ for Brazil ($N = 212 *10^6$). The blue solid line represents volatile empirical observer data and the orange solid line represents the multi-wave model calculation ($\lambda = 0.035$ day^{-1})

Centralized Management and Socio-Economic Contrast (Rhode Island, Figure 1): The method exhibits high approximation accuracy for both the total population and the dense Latino cohort. Two critical properties were identified. First, a pronounced phase shift requires shifting the epidemic start point t_0 for the Latino group to the left (earlier). This mathematically captures the cohort's occupational structure (essential workers with earlier exposure). Second, the extreme peak intensity for the Latino group (≈0.16%) vs. (≈0.05%) total) proves a "zero quarantine" regime under high household crowding. This rapid chain transmission minimized the derived attenuation parameter to a record low $\lambda = 0.0305$ day^{-1}.

Abrupt Macro-Systemic Shock (New York State, Figure 2): To test the pure wave geometry, the isolated first wave was plotted against the dimensionless time λ^*t, $\lambda = 0.0345$ day^{-1}. While the model accurately captures the maximum amplitude, the empirical trajectory shows a sharp structural asymmetry, peaking earlier $\lambda^*t \approx 1.9$ than the symmetrical analytical curve $\lambda^*t \approx 2.9$. This deviation identifies a fundamental boundary condition: an abrupt administrative shock (sudden lockdown) causes a non-linear collapse of the contact network, forcing an accelerated decay that the deterministic single-wave model naturally smooths out.

Structural Stochastic Chaos (Brazil, Figure. 3): Under decentralized regional management and fragmented testing, the empirical profile exhibits a prolonged, volatile multi-peak plateau. $\lambda = 0.035$ day^{-1}. The proposed framework successfully filters this noise by decomposing the

chaotic macro-profile into a sequence of three overlapping analytical waves, precisely capturing the transition minima at $\lambda^*t \approx 4.7$ and $\lambda^*t \approx 9.0$.

Thus, the algorithm functions as a robust mathematical filter, extracting invariant biological kinetics across all verified baselines—ranging from highly synchronized systems (Rhode Island) to network shocks (New York) and systemic structural chaos (Brazil).

Nevertheless, the deterministic solver successfully constrains the global amplitude and physical envelope across all three divergent populations. This close structural alignment validates the soundness of the simplified transmission operator, establishing a robust baseline for subsequent optimization and control analyses.

3.2. Effect of population age structure and intra-group contact patterns

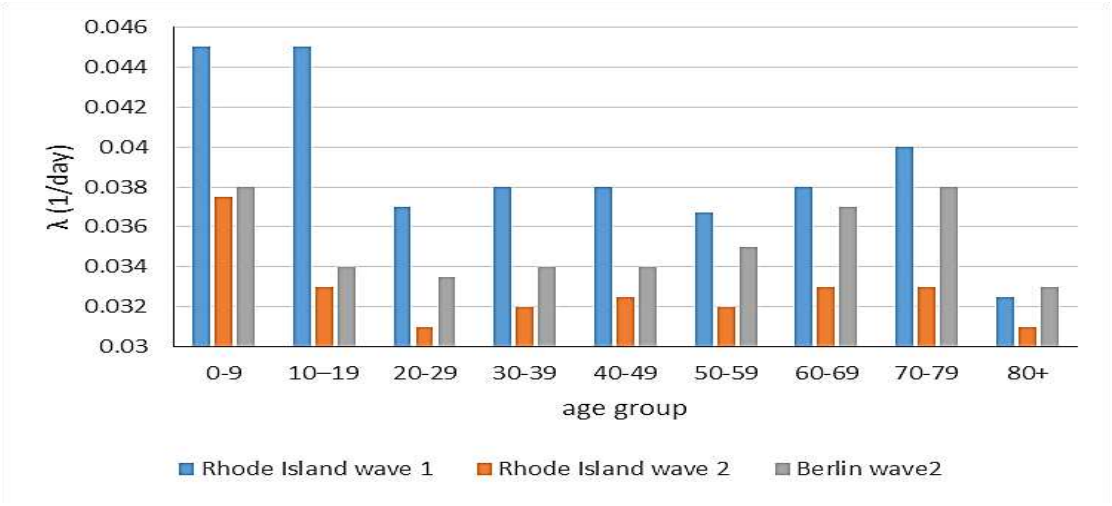


Figure 4. Empirical distribution of the behavioural containment rate λ (day^{-1}) across ten-year age cohorts for Rhode Island wave 1 (blue), Rhode Island wave 2 (orange), and Berlin wave 2 (grey)[4]. The asymmetric profiles highlight the structural divergence in containment efficacy between the high-mobility workforce (ages 20–29), insulated senior demographics (ages 60–79), and the structurally constrained oldest-old cohort (ages 80+).

To scale the deterministic transmission kinetics across disparate regional scales, the framework must incorporate age-stratified contact matrices. Localized outbreak velocities are heavily modulated by the intersection of demographic structures and age-specific compliance, as empirically quantified in Figure 4:

1. **The Behavioural Fatigue Shift:** During Rhode Island's first wave (blue), institutional lockdowns forced peak containment metrics ($\lambda \approx 0.045$ day^{-1}) in school-aged groups (0–19). In the second wave (orange), systemic fatigue collapsed these values uniformly to a low operational baseline ($\lambda \approx 0.031$ - 0.033 day^{-1}).
2. **The High-Mobility Core Minimum:** Across all cohorts—including Berlin's second wave (grey)—the young-adult demographic (ages 20–29) exhibits the absolute global minimum of containment ($\lambda \approx 0.031$ - 0.033 day^{-1}). This high-mixing workforce acts as the active transmission engine of the regional network.
3. **The Senior Insulation Rebound (60–79):** Older cohorts display a resilient rebound in compliance ($\lambda \approx 0.037$ - 0.040 day^{-1}), capturing strict targeted shielding behaviours and lower occupational contact requirements.
4. **The Vulnerable 80+ Drop:** Crucially, the oldest demographic (80+) exhibits a secondary, dangerous drop in λ down to the absolute systemic floor ($\lambda \approx 0.031$ day^{-1}). Rather than non-compliance, this drop reflects a structural baseline limit: the physical impossibility of cutting essential contacts, driven by reliance on healthcare networks, assisted living infrastructure, and multi-generational caregiving.

The share of the population aged 65+ (A(65+))is a separate demographic predictor of interest. Because more than 85% of COVID-19 hospitalisations and deaths occur in the 65+ age group, A(65+) is expected to capture the structural burden of severe outcomes independently of behavioural dynamics.

Before using λ and A(65+) as separate predictors of peak hospitalisation, we checked whether the two variables are sufficiently independent at the regional level. A strong association between them would indicate collinearity and would complicate the interpretation of their separate effects.

Linear regressions of λ on A(65+) gave:

Wave 1: $\lambda_1 = 0.0004 \cdot A(65+) + 0.0238$, $R^2 = 0.014$

Wave 2: $\lambda_2 = 0.00008 \cdot A(65+) + 0.0336$, $R^2 = 0.013$

In both waves the slope is positive but the explanatory power is very low ($R^2 \approx 0.014$). This near-zero R^2 indicates that A(65+) explains almost none of the regional variation in λ. The

two variables can therefore be treated as effectively independent predictors in the subsequent analysis of peak hospitalisation.

This independence is consistent with the heterogeneous behaviour within the 65+ group observed in Figure 4: λ increases for the younger part of this cohort (ages 60–79, reflecting stronger shielding), while λ decreases for the oldest-old (80+, reflecting a structural floor on reducing essential contacts). These opposing tendencies partially cancel out in the aggregate, weakening any linear association between A(65+) and λ.

Age structure and A(65+) capture the demographic component of heterogeneity, but the behavioural coefficient λ aggregates over socio-ethnic layers that are not uniform. Figures 5 and 6 illustrate the resulting divergence in infection trajectories and in λ across ethnic groups.

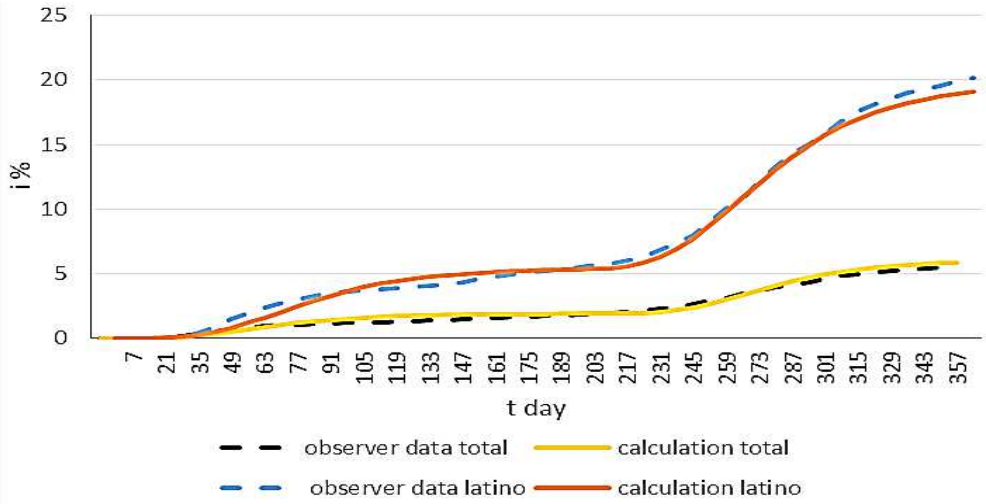


Figure 5. Long-term cumulative infection velocity (i % of the population) over a 360-day operational timeline. Dashed lines illustrate the empirical public health records (*observer data*) for the total population (*total*, black, N =1.057*10^6) and the high-contact demographic subset (*latino*, blue, N =1.59*10^5 [10]). Solid lines represent the corresponding closed-form deterministic trajectories (*calculation*, yellow and orange, respectively) generated by the modified transport engine. The dual-wave staircase topology highlights the breakthrough dynamics following behavioural compliance decay across independent temporal phases.

To fully resolve the multi-fold divergence in cumulative infection pathways, the macroscopic behavioural parameter λ must be disaggregated by socio-ethnic demographic layers (figure 6).

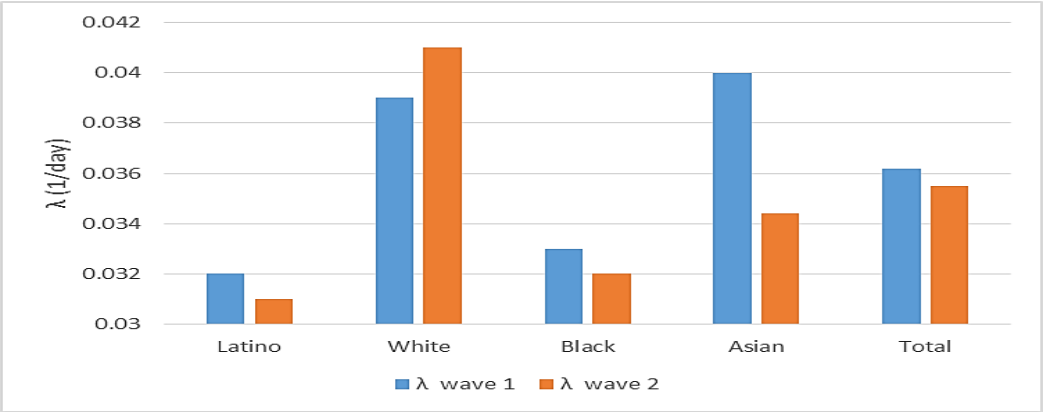


Figure 6. Empirical evaluation of the contact reduction parameter λ day^{-1} across localized demographic cohorts during wave 1 (blue) and wave 2 (orange). Traces compare *Latino*, *White*, *Black*, and *Asian* sub-populations against the integrated regional average (*Total*). The structural asymmetry highlights the socioeconomic constraints preventing uniform containment adaptation across frontline and multi-generational community layers.

The empirical data expose sharp structural divides in containment efficacy:

1. **The Structural Floor (*Latino* and *Black* Cohorts):** The *Latino* demographic exhibits the absolute minimum containment velocity $\lambda \approx 0.031$ - 0.032 day^{-1} across both waves. Similarly, the *Black* cohort is constrained to a suppressed baseline $\lambda \approx 0.032$ - 0.033 day^{-1}.Rather than voluntary non-compliance, this rigid floor reflects socio-economic imperatives, including over-representation in essential frontline workforces, dense multi-generational housing, and lower capacity for remote work. This ultra-low λ physically drives the rapid cumulative acceleration previously documented.
2. **The High-Insulation Segment (*White* Cohort):** Conversely, the *White* demographic displays peak containment metrics, which unexpectedly increase in the second wave $\lambda \approx 0.039$ to 0.041 day^{-1}, indicating an enhanced capacity for prolonged remote isolation and protective shielding.
3. **The Behavioural Decay Wave (*Asian* Cohort):** The *Asian* community demonstrates the most acute transition, dropping from peak ancestral compliance $\lambda \approx 0.031$ - 0.040 day^{-1} down to the regional mean $\lambda \approx 0.0345$ day^{-1} due to intervention relaxation and localized contact normalization.

This socio-ethnic stratification confirms that treating a metropolitan population as a homogeneous mixing field induces massive mathematical errors. The localized suppression of λ within the *Latino* and *Black* sub-groups forces their specific similarity invariants $\Pi_1 = k/\lambda$ directly into the explosive transmission zone $\Pi_1 \approx 2.5$.

Because these groups are linked to the broader urban network through essential economic sectors, they function as high-velocity core reservoirs.

3.3. Socioeconomic Determinants of Epidemic Control

Beyond demographic differences, the macroscopic resistance parameter λ\lambda may also be associated with structural socioeconomic conditions. Several socioeconomic and demographic variables were examined for their association with λ\lambda, including population density and other indicators of social status. Population density showed no substantial correlation with λ\lambda and was therefore not retained in the composite index. Variables exhibiting an absolute correlation coefficient above 0.3 with λ\lambda were considered for inclusion in the composite index.

Age structure was also examined separately because of its significant association with the macroscopic resistance parameter λ. Rather than incorporating age structure into the composite SES index, it was retained as an independent demographic factor to allow its specific contribution to epidemic control to be evaluated separately.

The resulting SES index is specific to the socioeconomic and demographic structure of the United States and is not intended as a universal socioeconomic indicator. Its components were selected according to the variables available and relevant within the US jurisdictional dataset; application to other countries would require a country-specific reformulation.

To explore this relationship, we define a composite Socioeconomic Status (SES) Index representing socioeconomic disadvantage:

$$SES = \frac{(Poverty * Uninsured * Latino)}{Education}$$

All constituent variables are expressed as fractions of the corresponding US national averages, such that higher index values represent greater socioeconomic disadvantage.

Jurisdictions with higher socioeconomic disadvantage exhibit lower estimated λ\lambda values. Ordinary least squares (OLS) regression against the logarithm of the composite index yields the empirical scaling relation:

$$\lambda = 0.0354 - 0.0015 * \ln(SES) \quad (17)$$

The observed association supports the interpretation of λ as a macroscopic parameter that may aggregate behavioural adaptation with structural socioeconomic constraints affecting the feasibility of contact reduction and NPI compliance.

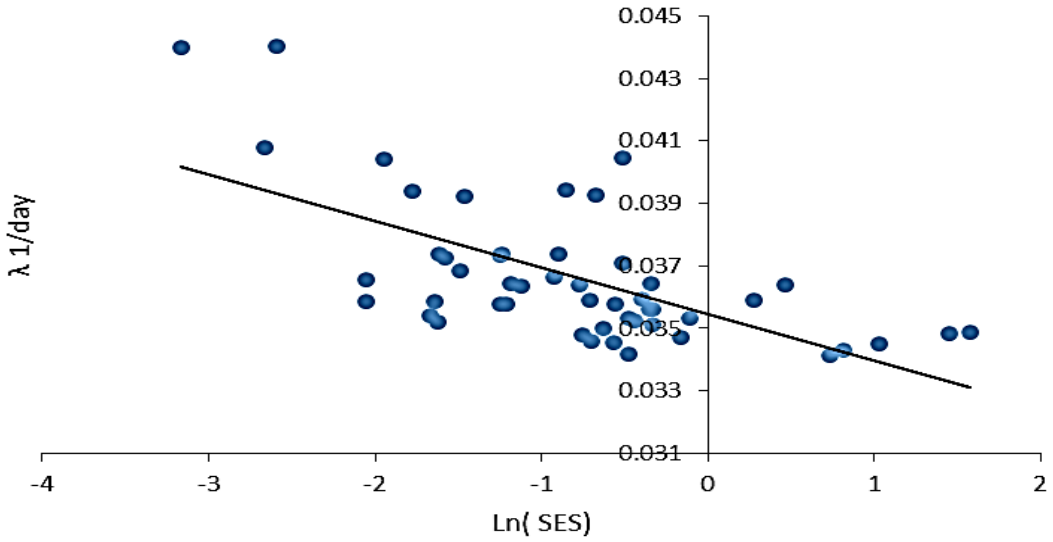


Figure 7. Macro-systemic association between the macroscopic resistance parameter λ and the logarithm of the composite Socioeconomic Status (SES) Index across 50 United States jurisdictions. The linear regression shows a statistically significant negative association ($r = -0.63$, $p<0.001$), with higher socioeconomic disadvantage associated with lower estimated values of λ.

4. Analytical estimation of peak hospital demand

This section develops an analytically tractable framework for estimating the peak number of hospital beds required during an epidemic wave.

4.1. Macroscopic mass balance

The dynamics of hospital occupancy follow a macroscopic mass balance tracking inflow and outflow of severe cases [11]:

$$dH/dt = \eta \cdot P(t) - \gamma \cdot H(t) \quad (18)$$

where H(t) is the bed occupancy, P(t) is the daily inflow of novel infections, η is the fraction requiring admission, and γ is the mean discharge rate (day^{-1}).

At peak utilization [11] dH/dt = 0, yielding:

$H_{max} = (\eta/\gamma) \cdot P_{max}$ (19)

4.2. Evolutionary Virulence-Transmissibility Trade-off Closure

For multi-wave applications, a relationship between the clinical admission fraction and the effective transmission coefficient may be introduced as a phenomenological closure:

$$\eta(k) = \eta_0 * \left(\frac{k_1}{k}\right)^{\mu} \qquad (20)$$

where η_0 and k_1 represent the baseline operational parameters of the ancestral strain, and μ denotes the evolutionary compromise exponent. Equation (20) is not a consequence of the similarity transformation itself. Rather, it represents an additional constitutive hypothesis introduced to close the hospitalization scaling across successive waves.

Substituting our closed-form analytical derivation for the peak incidence velocity into Equation (20) defines the universal scaling law for peak healthcare strain, where both sides are explicitly expressed as percentages of the total regional population (N):

$(H_{max} / N) * 100\% = (\eta / \gamma) * A(eff) * j_{max}$ (21)

where the relative maximum infection growth rate jmax = (Pmax / N) * 100% is determined by Equation (9), and A(eff) is the effective age modifier defined below (Equation 23a). After substituting Equation (9) into Equation (21), we derive the fully scaled analytical formulation:

$$\frac{H_{\max}}{N} * 100\% = \left(\frac{(\eta_0 * k_1^{\mu})}{\gamma}\right) * \lambda * A(eff) * k^{-\mu} * i_0 * \exp(\Pi_1 - 1) \quad (22)$$

4.3. Empirical estimation and healthcare calibration

The hospitalisation scaling relation was first evaluated without age-specific corrections, using empirical data from 50 US states across two pandemic waves. In this baseline formulation, the model produced moderate agreement for the first wave but substantially weaker agreement for the second, where optimisation converged to the maximum permitted lockdown level and modelled peak hospitalisation exceeded observed values by large factors, up to a factor of 7

for Utah. No corresponding increase in mortality was observed, indicating that the mismatch did not reflect a real excess of severe cases.

This discrepancy points to a structural limitation of the behavioural coefficient lambda as a sole predictor of hospital demand: lambda captures population-level contact behaviour but does not resolve the demographic composition of those contacts. Because more than 90% of COVID-19 hospitalisations and deaths occur among adults aged 65 and older, and because age-specific hospitalisation probabilities rise steeply with age, from 0.085 at ages 40–49 to 0.368 at ages 80+, a substantial fraction of infections in younger cohorts does not generate hospital demand. Treating all infections as equivalent therefore overestimates peak burden, especially when the age composition of infections shifts across waves.

The regional share of the population aged 65+ is not collinear with lambda. As established in Section 3.2, the two variables are effectively independent at the regional level ($R^2 \approx 0.013$–0.014), which justifies introducing age structure as an additional modifier in the scaling relation [12–14]. We therefore define the effective peak hospitalisation as:

$$H_{max}/N\ \% = \eta \cdot g \cdot A(eff) \cdot i_0 \cdot \exp(\Pi_1 - 1) \quad (23)$$

where η is the calibrated macro-parameter for healthcare burden scaling, $g = \lambda/\gamma$, and $\Pi_1 = k/\lambda$. The effective age modifier A(eff)is defined as:

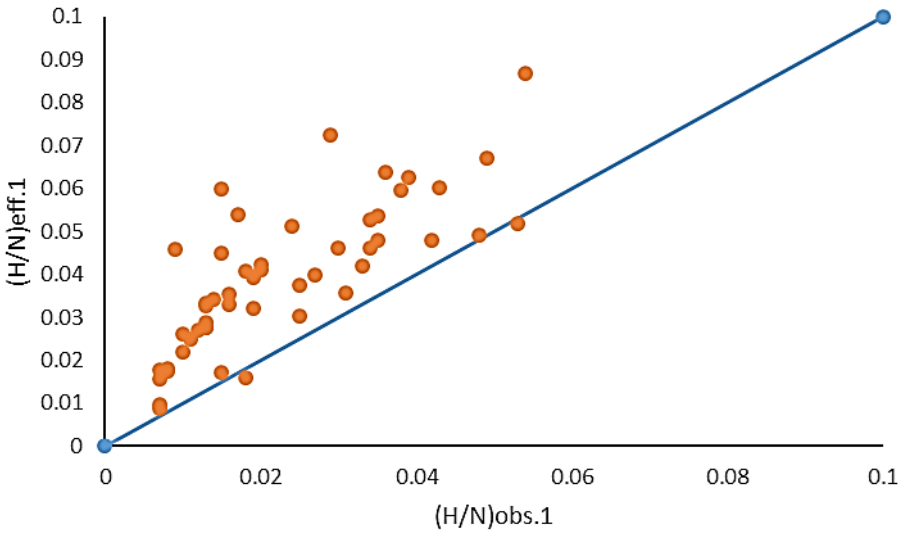
$$A(eff) = 0.85 * A(65+) + 0.15 * A(40–65) \quad (23a)$$

where A(65+) and A(40–65) are the regional population shares of the respective age groups. The weights 0.85 and 0.15 are normalised fatal-risk weights derived from the age gradient of case fatality, not from observed hospitalisation shares. With a US population share of approximately 0.31 for the 40–65 group, its additive contribution to Aeff is approximately 0.047, giving $A(eff) \approx 0.19$.

The formulation was calibrated separately for each wave using $\gamma = 0.167\ day^{-1}$ and $\eta = 1.474\%$ for Wave 1, and $\gamma = 0.238\ day^{-1}$ and $\eta = 1.146\%$ for Wave 2. Calibration was performed under the constraint of proportionality between modelled demand and observed delivery.

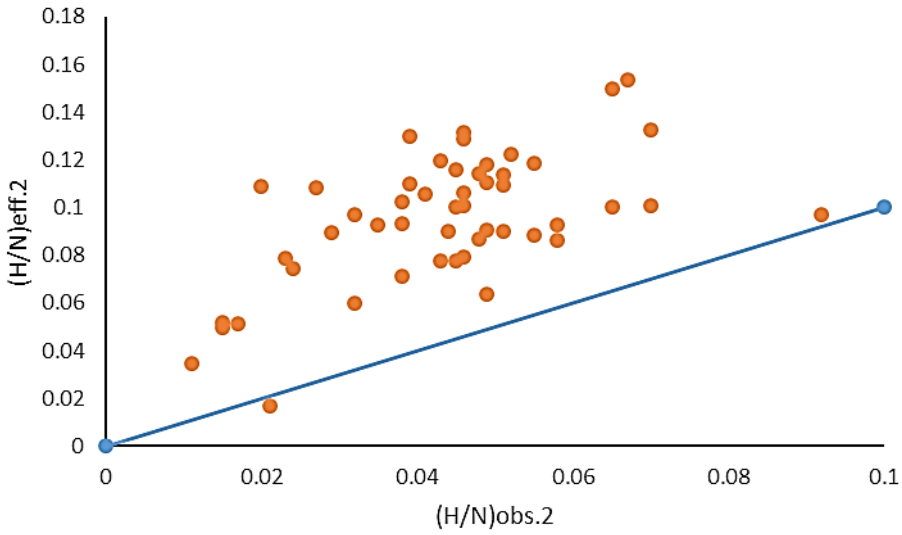
Peak bed demand is computed directly from Equation (23), not from an empirical fit to observed hospitalisation. The model does not seek to reproduce observed delivery, which is bounded by system capacity, but to estimate structural demand under the assumption that beds

457 are allocated according to age-specific fatal risk. We therefore do not report a regression
458 between modelled and observed values.



459

460 **Figure 8.** Modelled peak bed demand versus observed peak hospitalisation for the first wave
461 across 50 US states. Horizontal axis: observed (H_{max}/N)(obs) (%). Vertical axis: age-adjusted
462 model prediction (H_{max}/N) (eff) (%). The blue line represents proportionality (y = x). Points
463 converge towards the origin at low burdens and fan outwards at high burdens. No regression
464 line is shown. Model parameters: gamma = 0.167 day^-1, η = 1.474%, A(eff) = 0.85 * A(65+)
465 + 0.15 * A(40–65).



466

467 **Figure 9.** Modelled peak bed demand versus observed peak hospitalisation for the second
468 wave across 50 US states. Horizontal axis: observed (H_{max}/N) obs (%). Vertical axis: age-

adjusted model prediction (H_{max}/N)(eff) (%). The blue line represents proportionality (y = x). Points converge towards the origin at low burdens and fan outwards at high burdens. No regression line is shown. Model parameters: gamma = 0.238 day^{-1}, η = 1.146%, A(eff) = 0.85 * A(65+) + 0.15 * A(40–65).

In both waves, the scatter of modelled demand against observed hospitalisation converges towards the origin at low burdens and diverges upwards at high burdens. This pattern is consistent with the structural logic of the model: when load is low, capacity is sufficient and demand is met; when load is high, capacity becomes binding and the gap widens. The convergence towards the origin confirms that the model does not introduce a constant bias. The divergence at high burdens reflects capacity deficit, not model error.

The distribution of observed hospitalisation differs between the two waves: in the first, most jurisdictions clustered at 0.01–0.03% of population; in the second, the distribution shifted towards higher burdens, with increases of 2–3 fold for most states and 4–7 fold for some. The demand-to-delivery ratio is not constant: it rises from approximately 1.0 at low burdens to above 5.0 at high burdens, indicating that the deficit intensifies under strain.

At this initial stage of model development, we deliberately adopt a linear representation of the demand–delivery relationship. The available data do not support a reliable non-linear calibration, and a linear formulation preserves proportionality while avoiding overfitting of the structural deficit. We acknowledge that the scatter is not strictly linear and that a more detailed calibration would require independent measures of unmet demand, which were not available in the present study. This limitation defines a direction for future work.

4.4. Socioeconomic Scaling and Behavioural Decoupling of Peak Healthcare Strain

The macro-systemic scaling relation linking the calculated capacity strain with regional socioeconomic conditions was evaluated across 50 US jurisdictions. To enforce rigorous dimensional homogeneity and eliminate scale-dependent artifacts, both the dependent predictive parameter—the population-normalized peak hospitalization burden $\ln(H/N_{calc})$—and the independent predictor—the composite Socioeconomic Status Index ln(SES)—were evaluated using a unified natural logarithm base. The empirical evaluation reveals a profound structural divergence in the scaling laws governing the initial and subsequent pandemic phases.

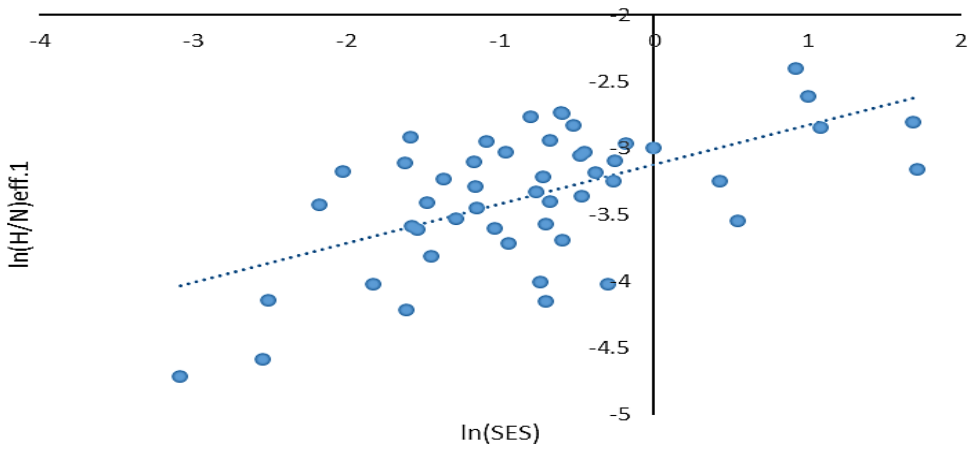


Figure 10. Macro-systemic scaling between the calculated peak hospitalization burden ln(H/N)eff.1 and the composite Socioeconomic Status (SES) Index across 50 United States jurisdictions during Wave 1. The ordinary least squares (OLS) regression demonstrates a robust, deterministic structural association ($R^2 = 0.348$), with the empirical scaling relation defined as:

$\ln(H_{max}/N)\ \text{eff.1} = 0.295\ \ln(\text{SES}) - 3.121.$

During Wave 1 (the ancestral pathogen surge), the system operates under a highly deterministic resource-constrained regime. The high goodness-of-fit confirms that during the initial unmitigated shock, regional socioeconomic vulnerabilities—specifically the rigid structural floor dictated by poverty, frontline occupational over-representation, and lack of health insurance—operated as the primary, unbuffered drivers of physical healthcare infrastructure strain. Conversely, during Wave 2 (the autumn-winter surge), the empirical system undergoes a critical structural decoupling. Running the identical OLS framework against the winter wave metrics results in a severe degradation of the linear baseline, with the socioeconomic index explaining only 11% of the observed variation ($R^2 = 0.11$), graph omitted for conciseness. This mathematical attenuation is not an error of the similarity framework, but rather a robust capturing of large-scale behavioural and institutional adaptation. Under the prolonged pressure of the winter wave, the population stratified along distinct psycho-social lines: wealthier, highly educated demographics (low SES cohorts) internalized the biological risk matrix, successfully mitigating hospitalization via proactive home-monitoring, private ambulatory tele-health networks, and voluntary hospital avoidance. Simultaneously, public health managers institutionalized highly effective financial and triage buffer pathways (notably via federal CARES Act provisions and targeted Medicaid hospital subsidies), allowing the acute care network to systematically absorb and stabilize lower-income cohorts. Consequently, this dual-driven behavioural mitigation compressed the

vertical distribution of the data points. The system effectively shifted from a purely structural, resource-constrained regime to an adaptively managed psychological matrix, successfully decoupling physical hospital demand from static socioeconomic baselines.

4.5. The Dimensionless Control (θ) and Lockdown Efficiency Operator (L)

To transition from micro-parameter forecasting to an operational policy framework, we introduce the dimensionless lockdown efficiency operator, L. We define L as the scale-invariant ratio of peak daily incidence velocity under interventions to the unconstrained biological baseline:

$$L = \frac{j_{\max(\lambda)}}{j_{\max(\lambda_{free})}} \quad (24)$$

where $\lambda_{free} = 0.031$ day^{-1} represents the system behaviour under zero institutional pressure (L = 1.0). Utilizing Equation (9), this operator maps the behavioural response directly into an exact physical mitigation metric:

$$L(\theta) = \vartheta * \exp\left[\left(\frac{k}{\lambda_{free}}\right) * \left(\frac{1}{\vartheta} - 1\right)\right] \quad (25)$$

where $\vartheta = \frac{\lambda}{\lambda_{free}}$ is the dimensionless control scaling parameter. Crucially, L(ϑ) is independent of the parameters η, γ, and N. Because the peak hospitalization burden scales as $H_{\max} \propto j_{\max(\lambda)}$, the operator satisfies:

$$L(\vartheta) = \frac{j_{\max(\vartheta)}}{j_{\max(\vartheta_{free})}} = \frac{H_{\max(\vartheta)}}{H_{\max(\vartheta_{free})}} \quad (26)$$

Thus, L(ϑ) simultaneously quantifies the reduction in both peak infections and peak hospitalizations relative to the unconstrained baseline.

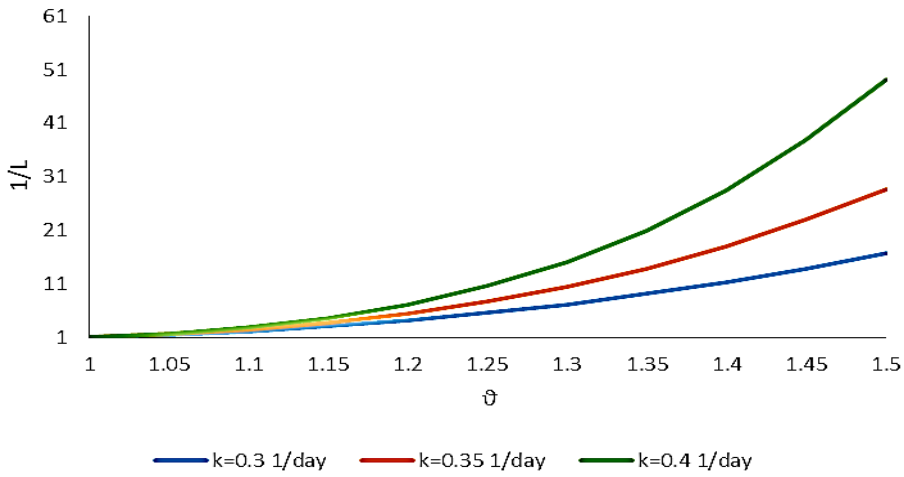


Figure 11. Non-linear scaling of the inverse lockdown efficiency operator. The damping metric 1/L(ϑ) plotted against the dimensionless control parameter k/λ_{free} ($\lambda_{free} = 0.031 day^{-1}$). The exponential trajectories illustrate the scale-invariant attenuation of peak hospitalization matrix intensity under institutional and behavioural pressure, independent of absolute regional capacity.

The analytical capacity of the inverse lockdown efficiency operator 1/L(ϑ) to scale up to factors of 30–40 is fully consistent with established empirical and epidemiological benchmarks. Macro-modelling frameworks of early-stage COVID-19 dynamics effectively demonstrated that aggressive, multi-layered suppression strategies can yield up to a 97% reduction in peak intensive care unit (ICU) and hospitalization demands relative to unmitigated biological baselines.

Phenomenologically, L(ϑ) aggregates the protective friction of physical distancing, contact minimization, and barrier prophylaxis, quantifying the reduction in social network conductivity. This formalizes how micro-scale behaviours adaptively damp transmission wave intensity. By reducing the effective transmission velocity without altering the intrinsic pathogen virulence, the operator L(ϑ) formally establishes the analytical boundary conditions required to evaluate state-level non-pharmaceutical interventions within unconstrained scaling laws.

5. Discussion

5.1. Generality, scalability, and implications for future epidemics

The analytical framework developed above is not confined to COVID-19. Its structure — based on dimensionless similarity invariants $\Pi_1$and Π_2— mirrors the logic of dimensional analysis used in fluid dynamics and heat transfer, where complex systems are reduced to a small set of governing dimensionless numbers. This enables a unified approach to epidemic forecasting across pathogens, regions, and time.

5.2. Macroscopic Interpretation and Socioeconomic Tuning of λ .

The resistance parameter λ represents the effective macroscopic damping velocity of epidemic transmission. It is not an arbitrary statistical curve-fitting coefficient, but a structural system parameter that aggregates population-level behavioural, demographic, and institutional processes. The empirical scaling relations established across 50 US jurisdictions confirm that λ is strongly modulated by a country-specific socioeconomic matrix. The robust deterministic coupling observed during Wave 1 (Figure 10) demonstrates that under an initial, unmitigated biological shock, the population's capacity for voluntary contact reduction is strictly bounded by material constraints. Frontline occupational exposure, high household crowding, and lack of healthcare insulation establish a rigid structural floor that prevents uniform NPI compliance in high-disadvantage (high SES) jurisdictions. Crucially, the severe degradation of this linear baseline during Wave 2 mathematically captures a behavioural phase transition. Rather than a failure of the similarity framework, this attenuation reflects non-stationary psychological and logistical normalization. Under prolonged pandemic pressure, high-income cohorts developed proactive risk-mitigation strategies (voluntary hospital avoidance, remote monitoring), while healthcare management adapted institutional and financial pathways to systematically stabilize lower-income groups. Thus, λ operates as a dynamic feedback operator, shifting the system from a purely resource-constrained regime to an adaptively managed psycho-social matrix.

5.3. Healthcare scaling and capacity ceiling anomalies

A principal operational application of the dimensionless framework is the deterministic translation of upstream epidemic wave kinetics into downstream population-normalised healthcare demand. The proportionality between modelled demand and observed delivery across jurisdictions supports the scale-invariant structure of the scaling law (Equation 22). However, the systematic divergence between modelled demand and observed delivery at the highest empirical burdens is of macroscopic significance. This deviation serves as a structural signature of the capacity ceiling effect: while the unconstrained demand model computes the

true volumetric need for hospitalisation, the observed data are truncated by physical and staffing limits.

The dimensionless strain index, defined as the ratio of calculated to observed hospital demand H(eff)/H(obs), reveals a clear macro-systemic pattern. During Wave 1, strain peaks dramatically in jurisdictions where biological demand outpaced admission capacity severalfold, indicating an unbuffered infrastructure shock. During Wave 2, the strain matrix shifts, exposing the effects of structural adaptation: severe escalation in some jurisdictions is driven by localised operational constraints, such as winter staffing shortages.

The strain ratios are not merely modelling constructs. Jurisdictions with the highest ratios — Utah (5.45), Idaho (4.02), New Mexico (4.00), and North Dakota (2.31) — are precisely those that formally activated crisis standards of care or documented hospital saturation during the second wave. Idaho activated statewide crisis standards on 16 January 2021 [15]. New Mexico implemented crisis standards on 11 December 2020 [16]. North Dakota and Utah declared all hospitals full on 9 and 8 November 2020 [17,18]. The model had no access to these declarations, and the correspondence between the ratio and independently documented capacity crises provides external validation that the model captures a real structural phenomenon.

The introduction of the age correction substantially changes this picture. Moving from the baseline formulation to the effective peak hospitalisation, defined through the A(eff) population share, improves the correspondence between model and observation for the second wave. While the baseline formulation systematically diverged from observed peak hospitalisation, the age-adjusted formulation brings modelled demand into closer agreement with observed delivery. This indicates that the combination of age correction and structural adaptation largely accounts for the observed peak hospitalisation burden. The remaining deviations are concentrated in jurisdictions with specific local constraints, rather than reflecting a systematic failure of the scaling law.

In Wave 1, by contrast, the scatter around the line of proportionality remains larger, consistent with the greater role of non-stationary factors during the first wave. The capacity ceiling effect is therefore most pronounced in Wave 1, while the second wave is better described once the age structure of hospitalisations is taken into account.

5.4. Generality Across Epidemic Systems

The similarity formulation is not intended to be specific to SARS-CoV-2. Its broader applicability across epidemic systems is examined in the companion study, where the same macroscopic methodology is applied to additional epidemic settings. The results provide complementary evidence for the use of similarity variables to compare epidemic trajectories with different transmission characteristics. The present study focuses specifically on the extension of this similarity structure to healthcare-demand scaling.

5.5. Open-System Extension

A structural limitation of the current framework is the assumption of macroscopically closed regional boundaries. In high-traffic socio-economic agglomerations, strict internal non-pharmaceutical restrictions cannot guarantee immunity from healthcare overload due to uncoupled cross-border viral diffusion. This is empirically illustrated by the State of California: despite early, rigid institutional mobility restrictions, intense inter-regional transit caused continuous external viral seeding, decoupling clinical utilization from localized compliance data.

Mathematically, the behavioural mitigation velocity λ is modelled as an endogenous response inversely proportional to the cumulative scale of local infection. However, in an open-system architecture, external viral injection artificially inflates the observed epidemiological growth, leading to a structural underestimation of localized compliance. To resolve this boundary condition without expanding the underlying parameter dimension, we introduce a scale-invariant transit modulusΩ_i:

$$\Omega_i = \frac{T_i}{T_{USA}} \qquad (27)$$

where T_i represents the pre-epidemic baseline interstate transit volume of state i, and T_{USA} denotes the aggregate national transport baseline. For highly connected open systems where $\Omega_i > 1$, the effective behavioural control parameter is adjusted via a linear boundary correction:

$$\lambda_{eff} = \lambda * [1 + \rho * (\Omega_i - 1)] \quad (28)$$

where ρ is the dimensionless cross-border diffusion sensitivity.

This formulation yields a critical operational policy insight: when systemic stress is driven by external injection ($\Omega_i >> 1$), further tightening of internal socio-behavioral restrictions (θ) yields diminishing returns and inflicts unnecessary macroeconomic dissipation. Under these

boundary conditions, the optimal managerial directive must shift from local mobility suppression to the direct attenuation of the transit modulus Ω_i via border screening and transport throttling, effectively restoring closed-system boundary conditions to stabilize the clinical infrastructure.

5.6. Limitations and Future Work

The present formulation has several limits of applicability. The single-wave approximation becomes less adequate when cumulative infection is no longer small relative to the effective susceptible population, requiring piecewise parameter updating or an extended coupled formulation. The treatment of vaccination is restricted to the mathematically admissible part of the vaccination trajectory, while successive epidemic waves are treated as sufficiently independent during the initial emergence of a new strain.

The analysis also treats each region as a macroscopically closed system. Highly connected regions may require an open-system correction to account for infection importation and transit effects, as outlined in Section 5.5. Future work should therefore examine time-dependent population resistance, explicitly coupled multi-lineage dynamics, and open-system effects using independent mobility and importation data.

An important further direction is to test whether controlled interventions in smaller, relatively homogeneous territories can provide quantitatively transferable information for larger populations when the relevant similarity conditions and boundary conditions are preserved.

The resistance parameter lambda represents aggregate population-level processes that reduce effective transmission. Its association with socioeconomic conditions is observational and does not establish causality.

Overall, the results support similarity variables as a macroscopic link between epidemic dynamics and healthcare demand. Further work should address time-dependent resistance, interacting lineages, open-system transmission, and mortality-based calibration of healthcare demand.

6. Conclusions

We have derived an explicit analytical expression for the peak hospital occupancy during an epidemic wave under combined non-pharmaceutical interventions and vaccination. The

solution is expressed in terms of two dimensionless parameters — Π_1 and Π_3 — which capture the intrinsic wave severity and the immunisation effort, respectively. This formulation enables rapid, simulation-free estimation of maximum bed demand for a wide range of scenarios.

An age-stratified modifier, A(eff), is introduced to account for the demographic composition of severe outcomes. The weights are derived from the age gradient of case fatality, reflecting the fact that hospital demand is concentrated among older cohorts. The resulting formulation reproduces the observed proportionality between modelled demand and delivered care across 49 US states, while also quantifying the gap between structural demand and actual delivery in jurisdictions where capacity was constrained. This gap is interpreted as capacity deficit, not model error.

The elasticity analysis demonstrates that, in the early acute phase of a wave, strengthening behavioural measures λ yields a substantially larger relative reduction in peak hospital burden than accelerating vaccination (v). However, vaccination remains critical for reducing disease severity, shortening hospital stays, and improving population-level outcomes over extended time horizons.

The framework provides a practical tool for healthcare planners to prioritise interventions based on prevailing epidemic conditions and capacity constraints.

Statements and Declarations

Declaration of generative AI and AI-assisted technologies in the writing process
during the preparation of this work the authors used ChatGPT to improve language clarity and check logical consistency. After using this tool, the authors reviewed and edited the content as needed and take full responsibility for the content of the published article.

Ethics approval: This study involved only the analysis of publicly available, anonymized COVID-19 aggregated data (incidence, hospitalizations, ICU occupancy). No individual patient data were collected, and no experiments on humans or animals were performed. Therefore, ethics committee approval was not required, in accordance with institutional and national guidelines.

Competing interests: The authors have no competing interests to declare that are directly or indirectly related to the work submitted for publication.

- Processed datasets, calculated dimensionless parameters, and regression matrices are available from the corresponding author upon reasonable request.

Data Availability

The empirical data supporting the findings of this study are publicly available from official sources. COVID-19 incidence data were obtained from official public health reports cited within the references. Hospitalization data were retrieved from the HHS/CDC COVID-19 Reported Patient Impact and Hospital Capacity dataset [14] and from the COVID Tracking Project[20].Historical demographic infection data for Rhode Island were sourced from the Rhode Island Department of Health (RIDOH) [10]; due to regional access restrictions, these specific wave-stratified datasets were verified and accessed via the Internet Archive Wayback Machine [19]. The processed datasets, calculated dimensionless parameters, regression matrices, and code used for model calibration and figure generation will be made available in a public repository upon acceptance and publication of the manuscript, or are available from the corresponding author upon reasonable request.

References

1. Kermack WO, McKendrick AG. 1927 A contribution to the mathematical theory of epidemics. Proc. R. Soc. A 115, 700–721. (doi:10.1098/rspa.1927.0118)-17
2. Anderson RM, May RM. 1991 Infectious Diseases of Humans: Dynamics and Control. Oxford, UK: Oxford University Press.
3. Sedov LI. 1959 Similarity and Dimensional Methods in Mechanics. New York, NY: Academic Press.
4. Below D, Mairanowski F. 2024 General patterns and differences of epidemic spread COVID-19. Arch. Med. Case Rep. Case Study 9(2). (doi:10.31579/2692-9392/211)
5. Planas D et al. 2022 Considerable escape of SARS-CoV-2 Omicron to antibody neutralization. Nature 602, 671–675. (doi:10.1038/s41586-021-04389-z)
6. Cele S et al. 2022 Omicron extensively but incompletely escapes Pfizer BNT162b2 neutralization. Nature 602, 654–656. (doi:10.1038/s41586-021-04390-6)
7. Dejnirattisai W et al. 2022 SARS-CoV-2 Omicron-B.1.1.529 leads to widespread escape from neutralizing antibody responses. Cell 185, 467–484. (doi:10.1016/j.cell.2021.12.046)

8. Gompertz B. 1825 On the nature of the function expressive of the law of human mortality, and on a new mode of determining the value of life contingencies. Phil. Trans. R. Soc. Lond. 115, 513–585. (doi:10.1098/rstl.1825.0026)-18
9. Dong E, Du H, Gardner L. 2020 An interactive web-based dashboard to track COVID-19 in real time. Lancet Infect. Dis. 20(5), 533–534. (doi:10.1016/S1473-3099(20)30120-1)-3-16
10. Rhode Island Department of Health. 2021 2021 Rhode Island COVID-19 Response Data Dashboard. See https://ri.gov (accessed 4 September 2026). Archived by Internet Archive Wayback Machine: https://archive.org.
11. Maki K. 2025 Methodology for predicting hospital admissions and evaluating recovery rates for coronavirus disease in Japan. PLOS ONE 20(10), e0334643. (doi:10.1371/journal.pone.0334643)
12. CDC. COVID-19–Associated Hospitalizations Among U.S. Adults — COVID-NET, October 2023–April 2024. *MMWR Morb. Mortal. Wkly. Rep.* **73**, (2024).
13. Griffin I, King J, Lyons BC, et al. Estimates of SARS-CoV-2 Hospitalization and Fatality Rates in the Prevaccination Period, United States. *Emerg. Infect. Dis.* **30**, 1144–1153 (2024).
14. HHS/CDC. COVID-19 Reported Patient Impact and Hospital Capacity dataset. Available from: https://healthdata.gov (accessed 25 July 2026).-4
15. Idaho Department of Health and Welfare. Crisis Standards of Care Activation, January 16, 2021.
16. New Mexico Department of Health. Public Health Order, December 11, 2020.
17. North Dakota Office of the Governor. Burgum announces steps to help with hospital capacity, November 9, 2020.
18. Utah Department of Health. Executive Order 2020-72: Declaring a State of Emergency Due to Rising COVID-19 Case Counts Creating a Shortage of Hospital Beds. Salt Lake City, UT: Office of the Governor; November 8, 2020.
19. Internet Archive. Wayback Machine. Available from: https://archive.org (accessed 25 July 2026).
20. The COVID Tracking Project. 2021 Hospitalized per million by state. The Atlantic Monthly Group. Available from: https://covidtracking.com (accessed 25 July 202